Surface states modulation of ZnTe via ultrathin ZnO layer as efficient photocathodes for CO_2 reduction reaction

Yan Wei, Yanbin Zhu, Peize Li, Xiaowu Gao, Zhaoshi Yu, Shujie Liu, Nan Li, Yan Shen [*], Mingkui Wang [*]

Wuhan National Laboratory for Optoelectronics, Huazhong University of Science and Technology, 1037 Luoyu Road, Wuhan 430074, Hubei, PR China

ARTICLE INFO

ABSTRACT

Surface states strongly affect charge transfer at the semiconductor/electrolyte interface and thus the total power conversion efficiency of photoelectrochemical CO_2 reduction. In this study, we report surface states modulation of ZnTe via ultrathin ZnO layer formed with a one-step hydrothermal method. The resulting photocathode achieved an impressive performance (-7.70 mA cm^{-2}, 93.88 % CO selectivity at -2.58 V vs. Fc$^+$/Fc) and stability (10 h) in CO_2-saturated acetonitrile with 0.1 M TBAPF$_6$ electrolyte. Detailed investigation including electrochemical impedance spectroscopy and DFT calculation reveals the surface modification of ZnTe with ultrathin ZnO layer reduces the energy disorder, thereby increasing the electron utilization involved in the CO_2 reduction reaction. This work provides an in-depth analysis of the charge transfer process at the semiconductor/electrolyte interface from the perspective of surface states and has the potential to stimulate further excellent research in this area.

1. Introduction

The photo-electrochemical (PEC) reduction of CO_2 has emerged as a promising avenue for concurrently addressing fossil fuels utilization and the associated CO_2 emission, while providing a sustainable route for fuel and chemistry production [1–3]. Thermodynamically, CO_2 reduction reaction (CO2RR) involves generating a highly negative potential intermediate (CO$_2^-$) at -1.9 V (vs. NHE) [4]. From the point view of electrode kinetics, a series of proton-coupled electron transfer (PCET) processes occur at the semiconductor/electrolyte interface (SEI) in solutions alongside a competitive reaction involving the two-electron process of H_2 evolution from H_2O. Given the intricate nature of these processes, the selection of materials for particular photocathodes is of paramount importance. Various semiconductor photocathodes, including p-Si [5], p-InP [6], Cu_2O [7], and $CuFeO_2$ [8], have been extensively studied, yet none have fully surmounted the inherent limitations. ZnTe has recently garnered attention as a promising photocathode material for PEC CO_2 reduction, owing to its significant negative conduction band edge position (-1.63 V vs. RHE) that exceeds the thermodynamic potential for producing a typical C1 compound from most CO_2 reduction processes, as well as a suitable electronic band gap of $\sim$2.23 eV [9,10]. The charge transfer onto ZnTe photocathode can be

successfully improved by doping with exteriors such as N and Al, or formatting Schottky junction with co-catalysts such as Au, and thus achieved remarkable increase in CO selectivity, photocurrent, and solar-to-fuel conversion efficiency [11–15]. Likewise, we introduced type-II g-C$_3$N$_4$/ZnTe heterojunction for photo-electrochemical CO_2 reduction to ethanol, highlighting the significant role of interfacial internal electric field in driving charge separation [16]. Nonetheless, a lack of microscopic understanding regarding charge transfer processes within the photocathode and at the SEI has limited the future application of ZnTe-based materials in PEC filed.

Theoretically, after excitation an abundant free-electrons in the conduction band of the photocathode generated by high-energy photons can transfer directly to CO_2 molecules through the SEI and thus promote the electrochemical reaction of CO_2 to CO [17,18]. Regarding for the PEC system in this study, the reaction primarily takes place at the SEI. Therefore, the effect from the bulk can be negligible in term of surface reaction [19]. The surface states (SS) at the semiconductor surface mainly origin from the dangling bonds and electronic states within the band gap [20,21]. At the very top surface of the actual ZnTe particles, the unsaturated Te dangling bonds could be generated due to lattice termination breaking the periodic crystal symmetry. In this study uses the terminology of SS to represent the dangling bonds for ZnTe. It is

[*] Corresponding authors.
E-mail addresses: ciac_sheny@mail.hust.edu.cn (Y. Shen), mingkui.wang@mail.hust.edu.cn (M. Wang).

well-documented that these high-valence Te dangling bonds locating nearly at the valence band maximum tend to act at the deep receptor level. For example, most of electrons show a tendency to transfer from semiconductors into electrolytes through the SS, i.e., an indirect charge transfer pathway involved in PEC CO_2RR. Due to their considerable abundance, the SS can serve as recombination centers and thus strongly affect charge transfer [22,23]. Thus, the SS play an important role in the interfacial charge transfer kinetics of the SEI, resulting in substantial charge recombination and energy losses [24–26]. The introduction of ultrathin insulating or wide bandgap oxides (e.g., Al_2O_3, Ga_2O_3, TiO_2, SiO_2) as the surface passivation layer or co-catalysts with catalytic function could reduce the content of SS and improve the charge separation/injection efficiency as well [27,28]. However, due to the complexity of the physicochemical nature of the photo-electrode interfaces, the charge transfer and collection mechanisms in these overlays remain unclear [29,30]. Moreover, in comparison with studies on SS in the field of PEC water splitting [31–34], the PEC CO_2RR has received relatively less attention. A recent study by Liu et al. utilized electrochemical impedance spectroscopy (EIS) and intensity-modulated photocurrent spectroscopy techniques to elucidate the function of SS onto the $CuIn_{0.3}Ga_{0.7}S_2$ photocathodes for PEC CO_2 reduction [35]. This revealed a noteworthy reduction in the SS concentration on the catalyst's surface when a mixed solvent of methanol and acetonitrile (ACN) was used. Therefore, a comprehensive examination of the photo-cathodic process on the SEI is highly desirable to gain deep insights into the SS and its impact on the PEC CO_2RR.

The present study reports the SS modulation of ZnTe via an ultrathin ZnO layer (noted as ZnTe@ZnO) in-situ formed with a simple one-step hydrothermal method. The n-type semiconductor material ZnO has been widely utilized for PEC application due to its transparency, highly conductivity, and facile fabrication [36–39]. The ZnO can effectively saturate the high-valence dangling bonds onto the surface of ZnTe due to their distinction in Fermi energy levels and element electronegativity. When used as photocathode for CO_2 reduction reaction, the ZnTe@ZnO exhibited a significantly improved PEC performance, showcasing excellent photocurrent density and stability in CO_2-saturated ACN solvents within a wide potential range. The detailed investigation further reveals that the presence of an ultrathin ZnO layer narrows the local state band tail by reducing dangling bonds on the ZnTe surface.

2. Experimental section

2.1. Synthesis of the ZnTe@ZnO photocathodes

All chemicals used in this study were of analytical grade and used without further purification. The ZnTe@ZnO photocathodes were synthesized on the zinc substrate by a simple one-step hydrothermal method. 4 cm × 2 cm sheets of zinc were polished and cleaned with low concentrations of sulfuric acid to remove surface oxides for tellurisation reaction. The polished zinc substrate was placed at an angle against the wall of Teflon-lined autoclave reactor (volume 100 mL). The mixture of $NaTeO_3$ and $NaBH_4$ with different molar ratio (5:1, 10:1, 20:1, 40:1, 80:1, and 160:1) in 30 mL of Milli-Q water was stirred continuously under nitrogen for 15 min, respectively. The precursor solution was transferred into the reactor as described above. The sealed autoclave was heated at 195 °C for 3 h in an oven and allowed to cool naturally to room temperature. ZnO samples actually do not add $NaTeO_3$ raw materials during its synthesis process. Table S1 lists the ZTO-X samples (where X represents the molar ratio of raw materials $NaBH_4:Na_2TeO_3$ ranging from 5 to 160).

2.2. Material characterizations

The morphology and composition of the synthesized ZnTe@ZnO were studied by Scanning Electron Microscope (SEM, HITACHI S4800) and transmission electron microscopy (TEM, Tecnai G2 F30 S-TWIN),

which was equipped with energy dispersive X-ray (EDX) spectrometer. The crystal structure of as-synthesized samples was analyzed by x'pert3 powder X-ray diffraction (XRD) with Cu-Kα radiation. The diffraction patterns were recorded in the range of 20 to 70, and the grazing incidence angle = 1°. X-ray photoelectron spectroscopy (XPS) was used to determine the valence band position by using AXIS-ULTRA DLD X-ray photoelectron spectrometer. Photoluminescence (PL) spectra were scanned on a photoluminescence spectrometer (FLS920, Edinburgh Instruments Ltd.) from 400 to 700 nm under an excitation wavelength of 325 nm. The isotope labelled gas was analyzed by gas chromatography-mass spectrometry (PerkinElmer Clarus 690, Clarus SQ 8 T GC).

2.3. Photoelectrochemical experiments

Photoelectrochemical (PEC) experiments were carried out on an electrochemical workstation (CHI 650c) at room temperature with an airtight, three electrode quartz H-type photoelectrochemical cell. Herein, a saturated calomel electrode (SCE) was used as the reference electrode and the ferrocenium/ferrocene (Fc^+/Fc) couple was used as the internal potential reference and a Pt sheet as a counter electrode. A 300 W Xe lamp (Newport 66921) with an AM 1.5 G filter was used to simulate solar illumination, and the light intensity was adjusted to 100 mW cm^{-2} by calibration with NREL-calibrated silicon solar cells. The photo-activated CO_2 reduction was measured under chopped illumination for observing the photo-response under dark and light simultaneously. The photocurrent was measured by linear sweep voltammetry with a scan rate of 10 mV s^{-1}. The incident photon conversion efficiency (IPCE) was obtained under irradiation from single bandpass light of a different wavelength generated by monochromatic filters. The gaseous products (CO and H_2) were identified by with an inline gas chromatograph (A91plus PANNA) equipped with flame ionization detectors (FID) and thermal conductivity detector (TCD). Nitrogen (99.999 %) was used as the carrier gas. Liquid products were analyzed on a Bruker AscendTM 600-MHz NMR spectrometer. A 0.3-mL sample of the electrolyte was mixed with 0.2 mL CD_3CN in which 1 mM dimethyl sulphoxide was added as an internal standard. Impedance measurements were carried out on the potentiostat with frequency ranges from 5 MHz to 0.2 Hz and a 25-mV sinusoidal amplitude.

3. Results and discussion

Scheme 1a illustrates the energetic diagram of a ZnTe photocathode working under stationary conditions for CO_2 reduction. The presence of defect states could be caused by Te dangling bonds within the bulk ZnTe band gap above the Fermi energy level EF as indicated by the projected density of states (PDOS) in Fig. S1[40]. Due to the existence of donor-like SS onto the surface, holes from the valence band tend to fill up the SS above the Fermi-level in order to establish thermal equilibrium, causing the band bending in the space charge region. Here, it is assumed that the SS functions as a carrier recombination site, i.e., the recombination at the interface takes place via the SS. (Scheme 1a). Under illumination, the excess of photogenerated electrons in the p-type semiconductor leads to stationary nonequilibrium conditions, and hence to different free energies of the charge carriers as given by quasi-Fermi level of E_{Fn} for electrons and E_{Fp} for holes. The introduction of ZnO layer onto the ZnTe photocathode surface could modulate of the distribution of SS (described as energy disorder σ in Scheme 1b) and thus increase the partial cathodic current flux in the first pathway for PEC CO_2 reduction (Scheme 1a). It is worth noting that, rather than an increase in number of photogenerated carriers, this improvement could be attributed to a decrease in energy disorder (σ). This is particular true for redox processes to be discussed later.

We first carried out density functional theory (DFT) calculations on the charge density difference between the ZnTe and ZnO to evaluate the possibility of interfacial charge transfer in the ZnTe@ZnO heterogeneous structure. Fig. S2 illustrates the most stable ZnTe@ZnO stacking
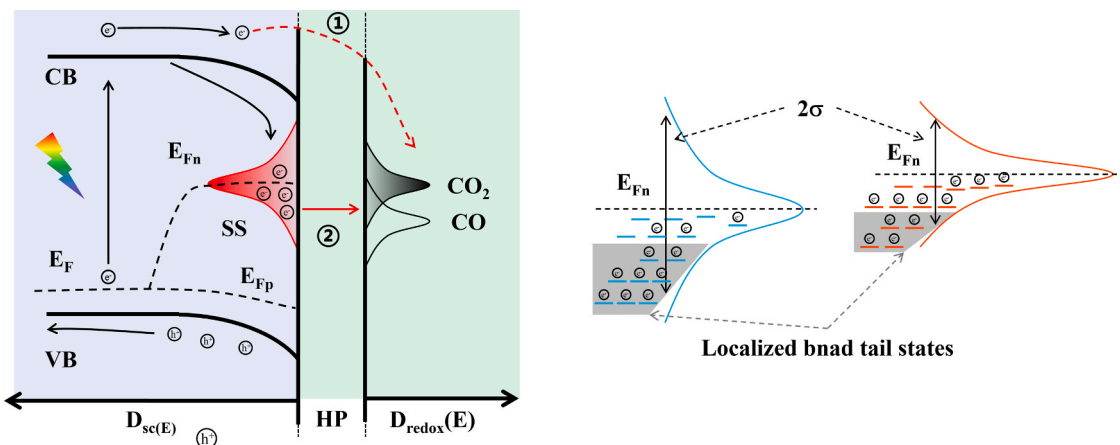
Scheme 1. (a) Energy band diagram of a photoelectrode for CO_2 reduction to CO. Electron extraction from the conduction band of a p-type semiconductor into an oxidant (CO_2 herein) indicated as the first pathway and the recombination pathway. Surface state-mediated route is shown for the recombination. Surface states mediation of both minority carrier (i.e., electron) transfer and recombination for a p-type semiconductor electrode interface. (b) Modulation of surface states by reducing the disorder.

model. The three-dimensional charge density difference between the ZnTe and ZnO of ZnTe@ZnO in Fig. 1a suggests a charge redistribution close to the interface of ZnTe@ZnO, in which the colors blue and yellow represent charge dissipation and accumulation, respectively. Specifically, Fig. S3 shows the average planar electron density difference of them along the Z direction. The change of charge density at the interface between ZnTe and ZnO indicates that when ZnTe is tightly contacted with ZnO, the electrons are prone to flow into ZnO from ZnTe via the interface. This electron flow is driven by the disparity in the Fermi energy levels between ZnTe and ZnO, resulting in establishment of a built-in electric field directed from ZnO to ZnTe at the interface (Fig. S4 and S5). The interfacial distance between ZnTe and ZnO was measured to be less than 0.27 nm. This was determined by measuring the average position of Te atoms on the outermost surface of ZnTe and the average position of O atoms on that of ZnO. Bader charge analysis was conducted to gain a quantitative understanding of the charge transfer, showing the transfer of approximately 0.45 |e| at the ZnTe@ZnO interface. Likewise, Fig. 1a depicts the transfer occurs via the interfacial Te-Zn bond. This significantly reduces the number of lone-pair electrons in the high-valence state of Te on the pure ZnTe surface and significantly promotes the directional charge separation on ZnTe@ZnO.

We further performed DFT calculations to investigate and compare the Gibbs free energies (ΔG) of the main species involved in CO_2 reduction on ZnTe and ZnO surfaces (Tables S2 and S3). Fig. 1b shows the ΔG values for the intermediates (*COOH and *CO) on the ZnTe (111) or the ZnO (002) surfaces. ZnTe (111) and ZnO (002) surfaces have the

same rate-determining step of *COOH formation, implying that the enhanced adsorption of *COOH would reduce the formation barrier and accelerate the catalytic reaction. The ΔG value of COOH* formation is 0.98 eV for the ZnTe (111) surface, which is higher than that of the ZnO (002) surface ($\Delta G = 0.79$ eV). Thus, introducing a ZnO layer onto the photocathode surface could achieve a superior electrocatalytic activity to the ZnTe due to its lowest uphill. This observation suggests that ZnO is a promising electrocatalyst material for CO_2RR [41,42]. Thus, The COOH* intermediates are more likely to form on the surface of the ZnO (002) than the ZnTe (111), i.e., an activation of CO_2 on the ZnTe catalyst surface is enhanced by the introduction of a thin layer of ZnO with a higher activity. Furthermore, in comparison to the Te-C site in the ZnTe-COOH adsorption state, a noticeable charge accumulation region at the O-C site is observed in the differential charge density of the ZnO-COOH adsorption state (Fig. S6). This includes a shorter bond length, signifying an enhanced adsorption of *COOH on the ZnO surface. The observed distinction is likely attributable to differences in adsorption atom sites.

Based on these theoretical investigation results, we further synthesized ZnTe@ZnO for PEC CO_2 reduction. Fig. S7 illustrates the synthesis protocol of ZnTe@ZnO samples, which involves two main procedures, i. e., tellurisation followed in-situ wrapping of zinc oxide. The success of growing a layer of ZnO on the ZnTe surface can be ensured by the fact that the solubility product constant (K_{sp}) of ZnO (6.8×10^{-17}) is much larger than that of ZnTe (5.0×10^{-34}) in water [43], and by the presence of an excess amount of $Zn(OH)_4^{2-}$ produced during the synthesis of ZnTe
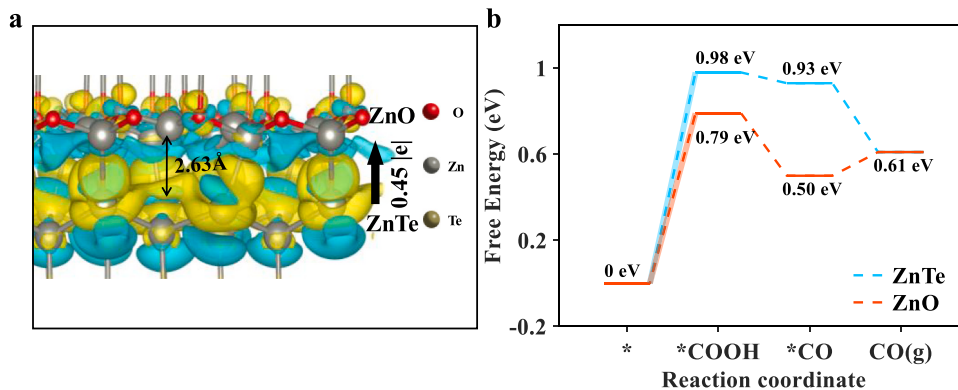
Fig. 1. (a) Three-dimensional charge density difference of ZnTe@ZnO sample. The value of isosurface is set to 0.0013 ebohr^{-3}. (b) The calculated free-energy diagrams of CO_2 reduction reaction to CO onto ZnTe (111) and the ZnO (002) surfaces.

and ZnO [44]. ZnO was synthesized onto zinc substrate according to previous reported method [45]. The detailed description of reaction process is given in the supporting information.

Our investigation began with grazing incidence X-ray diffraction (GIXRD) analyses on ZnTe@ZnO samples by varying the ratio of $NaBH_4$: Na_2TeO_3 from 5:1 to 160:1 as shown in Fig. 2a and Fig. S8. Clearly, the distinctive diffraction peaks ($2\theta = 25.3°$, $29.2°$, $41.8°$, and $49.5°$) aligned with the zinc-blende ZnTe phase clarify the successful synthesis of the pure ZnTe phase in samples. The raw material ratio changes from 5:1 (ZTO-5) to 20:1, and the synthesized samples are all ZnTe phase. Meanwhile, as the raw material ratio changed from 40:1 (ZTO-40) to 80:1 and 160:1 (ZTO-160), there was a gradual increase in the intensity of the 2θ XRD peak at $34.4°$, while the intensities of the peaks at $25.26°$ and $41.91°$ gradually decreased, and no significant shift of the diffraction peaks was observed. This observation indicates the appearance of ZnO crystal peak (002) and a corresponding weakening of ZnTe crystal peaks (111) and (220) on the surface. In the absence of a Te source, only the ZnO phase was observed, and no ZnO was present in the polished zinc sheets (Fig. S9).

A typical scanning electron microscopy (SEM) image of ZTO-80 in Fig. 2b shows a heterogeneous, polygonal prism-like ZnTe structure enveloped by strawberry seed-like ZnO (red circle). Notably, the surface roughness became intensified as the raw materials ratio ($NaBH_4$: Na_2TeO_3) increases from 5 to 160 (Fig. S10), possibly due to a continuous growth of ZnO particles onto the initial layer. The high-resolution transmission electron microscopy (HRTEM) image of ZTO-80 in Fig. 2c clearly shows lattice fringes, and there is no obvious lattice distortion in them. The interplanar spacings of 0.355 nm and 0.260 nm corresponds to the (111) plane of ZnTe and the (002) plane of ZnO. We used the white dashed line to distinguish the ZnTe-ZnO interface and confirm the heterojunction formed in samples. This indicates an ultrathin ZnO layer fully covering ZnTe particles. The high-angle annular dark-field scanning TEM (HAADF-STEM) images and energy dispersive X-ray spectroscopy (EDX, Fig. S11) also support this point.

We further carried out X-ray photoelectron spectroscopy (XPS) analysis to determine the surface elemental composition and the chemical states of ZnTe and ZTO-80 samples. Fig. 2d presents the XPS spectrum for Te_{3d}. The observed two distinct peaks at the binding energy of 586.83 eV and 576.43 eV for the sample of ZnTe can be assigned to the Te^{4+} species, verifying the presence of a few amounts of Te^{4+} due to Te dangling bonds [16,46]. It is notable that by covering an ultrathin layer of ZnO on ZTO-80, the XPS signal intensity at the binding energy of 586.83 eV and 576.43 eV decreases. Accordingly, the content of Te^{4+} species in the ZTO-80 sample dropped from about 9 % to 4 %, compared to the ZnTe sample (Table S4). This could be contributed to the incorporation of ZnO layer to repair the surface fractures and saturate the dangling bonds. Furthermore, we noticed that the binding energy of the Te $3d_{3/2}$ for the ZTO-80 shifted positively by 0.17 eV in comparison with the ZnTe sample. In line with the observation, the XPS binding energy of the Zn 2p for the ZTO-80 shifted negatively by 0.05 eV in comparison with the ZnTe sample (Fig. S12). The above-mentioned charge transfer tendency is consistent with the DFT calculations [47].

We conducted linear sweep voltammetry (LSV) measurements on various samples to assess their PEC performance in CO_2-saturated ACN containing 0.29 vol% water with 0.1 M $TBAPF_6$ under chopped AM 1.5G solar simulated light. The effect of water content was also tested (Fig. S13). The ZTO-80 electrode exhibited the highest photocurrent in Fig. S14. This is mainly due to the fact that too thick ZnO growth eliminates the built-in potential, thus, the driving force for the carrier separation. Therefore, we selected the ZTO-80 sample as the target photocathode in the following investigation without special remark. Previous study has established that the introduction of a small quantity of water into organic aprotic solvents can significantly amplify the photocurrents and uphold the elevated CO selectivity [48–50]. Fig. 3a shows the LSV curves of the ZnTe@ZnO (i.e., ZTO-80) photocathode in CO_2-saturated ACN under chopped AM 1.5 G illumination. Comparative saturated N_2 and CO_2 experiments and isotopically labelled carbon dioxide ($^{13}CO_2$) tests determined that the main reason for the increase in photocurrent is the reduction of CO_2 to CO gas (Fig. S15). The ZnTe or ZnO individual electrode was also tested for comparison purpose. The ZTO-80 photocathode showed an exceptionally strong photocurrent of -7.7 mA cm^{-2} at -2.58 V (vs. Fc$^+$/Fc), being 2.75 times of the ZnTe
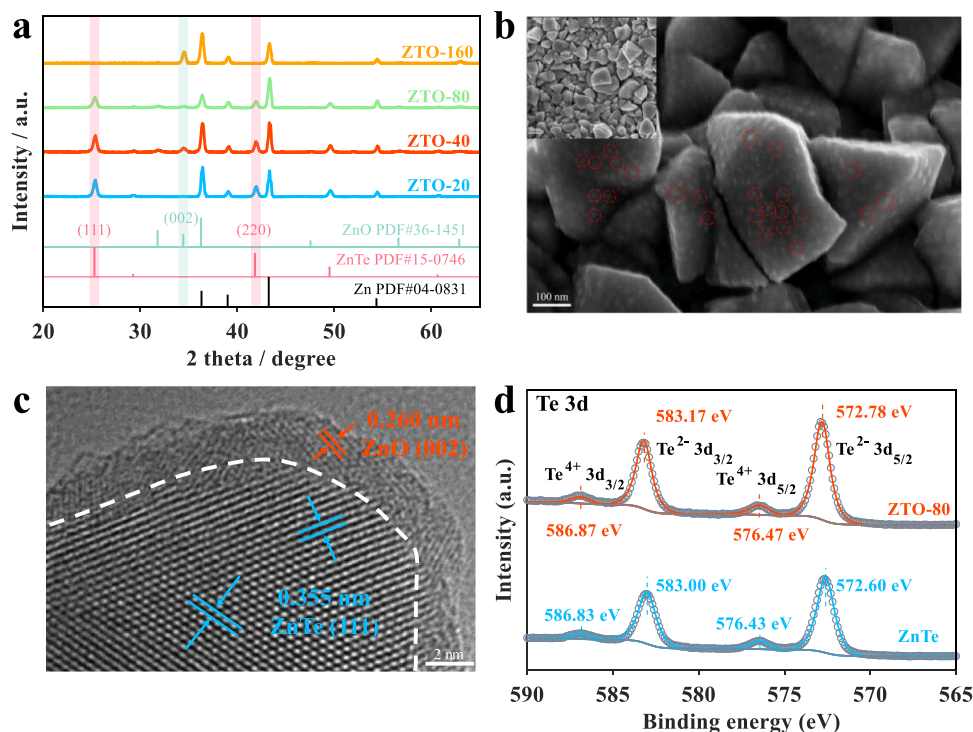
Fig. 2. (a) GIXRD patterns of the ZTO-X samples (where X represents the molar ratio of raw materials $NaBH_4$:Na_2TeO_3 ranging from 20 to 160). (b) SEM and (c) HRTEM images of the ZTO-80 sample. (d) High-resolution XPS spectra for Te 3d of the as-synthesized samples.
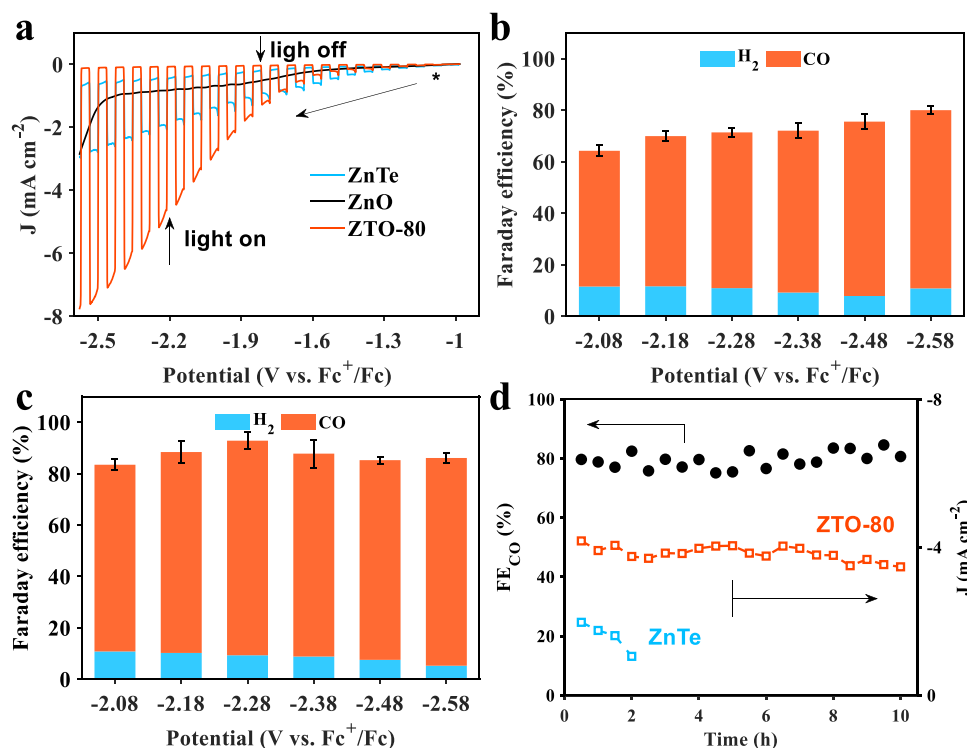
Fig. 3. (a) LSV curves of the ZTO-80, ZnTe, and ZnO photocathodes at a scan rate of 10 mV s^{-1}. The faraday efficiency (FE) at different applied potentials for (b) the ZTO-80 and (c) the ZnTe photocathodes. (d) Long-term stability test (left coordinate: Faraday efficiency for CO; right coordinate: current density) of the ZTO-80 photocathode and ZnTe photocathode at − 2.28 V vs. Fc$^+$/Fc. All test measured in CO_2-saturated acetonitrile (ACN) containing 0.29 vol% water with 0.1 M TBAPF$_6$ under chopped AM 1.5 G (100 mW cm^{-2}) illumination.

electrode (−2.8 mA cm^{-2}). This may be related to the Fermi-level pinning effect [40,51]. In contrast, the ZnO electrode exhibited an invisible photocurrent, mainly due to its typical n-type semiconducting property. The monochromatic incident photon-to-current efficiency measurements further confirm the superiority of ZTO-80 electrode (Fig. S16). Besides, ZnO shows a significantly higher dark current compared to ZnTe and ZTO-80 (Fig. 3a) and the high CO selectivity (Fig. S17 and S18) suggests that this is an electrocatalyst material for CO_2RR.

The main products of PEC CO_2 reduction on both photocathodes were gaseous CO and H_2 as confirmed by GC characterization. No liquid products were detected by NMR spectra. Figs. 3b and 3c compares the faraday efficiency (FE) of PEC CO_2 reduction on the ZTO-80 and the ZnTe photocathodes at different potentials (from −2.08 to −2.58 V vs. Fc$^+$/Fc). As for the ZTO-80 photocathode, the PEC CO_2RR to CO achieved a higher FE over 70 % in the entire potential range. Those values are almost 10–20 % higher than the ZnTe photocathode. It is notable that both photocathodes exhibited similar FE of H_2 (< 10 %). Specifically, for the ZTO-80 photocathode, the total FE of CO reaches a maximum value of 84 % at − 2.28 V (vs. Fc$^+$/Fc), together with a high overall selectivity of 90 % for CO. Instead, the ZnTe electrode showed a lower total FE value of 60 % and a lower selectivity of 85 % at the same potential. This phenomenon, where the total FE falls short of 100 %, may be attributed to electron consumption in the photocorrosion[12,35,52]. Interestingly, the incorporation of ZnO could effectively mitigate this photocorrosion, consequently augmenting the total FE. The Solar-to-CO efficiency (η_{STC}) of the ZTO-80 photocathode reached 6.0 % at − 2.28 V (vs. Fc$^+$/Fc) under AM 1.5 G irradiation (100 mW cm^{-2}), being 4.3 times of the ZnTe electrode (1.4 %) [15]. Our investigation indicates that the ZTO-80 electrode possesses a remarkable photocatalytic activity for the PEC reduction of CO_2 to CO, offering it one of the most efficient photocathodes reported so far in organic solvents (Table S5).

The CO gas yield rate on the ZTO-80 electrode reached 261.47 μmol

cm^{-2} h^{-1}, which was 2.8 times higher than the ZnTe electrode's rate of 93.55 μmol cm^{-2} h^{-1} in Fig. S19, aligning with the improved CO selectivity observed in Fig. 3b and c. The stability assessment was conducted by monitoring the FE of CO products and the photocurrent on the ZTO-80 sample over a 10-hour span at − 2.28 V (vs. Fc$^+$/Fc) under AM 1.5G light. As shown in Fig. 3d, the photocurrent density (absolute value) decreased by about 17 % from an initial value of − 4.17 to − 3.47 mA cm^{-2} after 10 h, while the FE value of the CO product was kept stably at about 80 % without significant degradation. In contrast, the ZnTe photocathode exhibited severe photo-corrosion behavior within 2 h of testing, as reflected by a significant 46 % decrease in photocurrent. The SEM image in Fig. S20 reveals a transformation in the fundamental morphology of ZnTe, forming a flocculent structure in contrast to ZTO-80. Additionally, XPS analysis in Fig. S21 indicates oxidation of ZTO-80 after stability measurement, with a gradual rise in Te^{4+} content observed during extended photochemical testing, consistent with findings in the literature [53,54]. These findings collectively indicate that the surface modification involving an ultrathin ZnO layer on the ZnTe electrode effectively mitigates photo-corrosion, bestowing the enhanced PEC performance.

We further carried out EIS characterization on these photocathodes to monitor the changes in resistance and capacitance correlated with the SS in terms of charge trapping and charge transfer under illumination. In contrast to the typical electrochemical setups in Fig. S22a, model, as depicted in Fig. S22b, points out the pivotal role of SS as recombination centers [55]. Here, $C_{ct,ss}$ represents the capacitance of the electron-hole complex recombination center, in parallel with $R_{ct,trap}$ which depicts the charge transfer process from the SS to the redox couple. Considering the actual electrode surface specifics, $CPE_{ct,ss}$ is chosen to replace $C_{ct,ss}$. Fig. 4a shows a typical graphical analysis of impedance spectroscopy in a Nyquist plot. The resistance and capacitance associated with charge transfer at the SEI can be assessed by fitting the impedance curve with the model shown in the inset. The model fits our data well. Fig. 4b shows
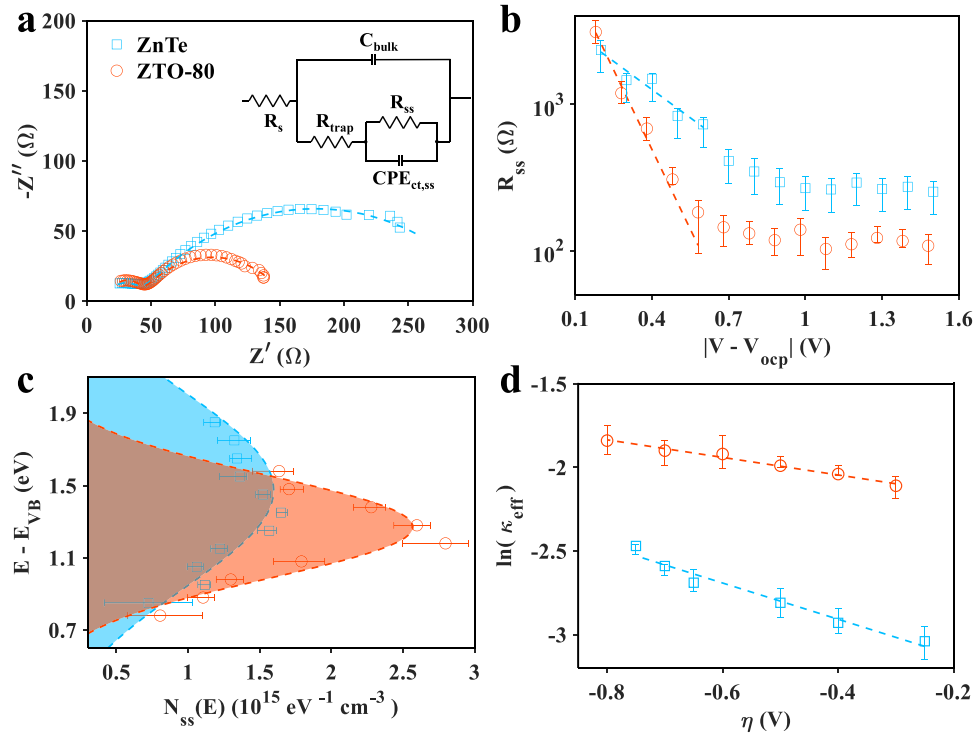
Fig. 4. (a) The electrochemical impedance spectroscopy (EIS) measurement of the ZnTe and the ZTO-80 samples. The EIS measurement was done over a frequency range of 10^5–0.1 Hz and at an amplitude of 10 mV. (b) The obtained R_{ss} as a function of applied potential for the ZnTe and the ZTO-80 photocathodes. (c) The DOS of SS as a function of the applied energy offset with respect to the valence band edge for ZnTe and ZTO-80 photocathodes derived from the $CPE_{ct,ss}$, the conversion of potential and energy refer [40]. (d) The plot of $\ln(\kappa_{eff})$ vs. η for the ZTO-80 and ZnTe photocathodes under blue light illumination in 2 mM $Fe(C_5H_5)_2$. The square data represents ZnTe photocathodes, the circle data represents ZTO-80 photocathodes and the dotted line indicates the fitted.

the charge transfer resistance R_{ss} of the two photocathodes at different potentials. According to the Gerischer model [56], electrons trapped by the SS and are hindered from participating in the solution-based reaction under a low applied bias. As the applied voltage increases, electron transfer from the conduction band or the SS to the unoccupied electron levels to facilitate the redox reaction with species in the electrolyte (CO_2 → CO) [40]. Therefore, the interfacial electron transfer resistance is exponential to the potential based on the electronic Fermi level as described by Eq. (1) (i.e., in the range the electron energy level being far away from the conduction band).

$$R_{ss} = R_{ss,o}\exp\left[-\frac{q\beta}{K_BT}V\right] \tag{1}$$

where $R_{ss,o}$ is a constant, and the voltage V here takes the open circuit voltage as a reference value. Consequently, the electron transfer coefficient β for the semiconductor electrodes detailed in the ZnTe and ZTO-80 electrodes can be determined to be 0.07 and 0.17, respectively. The parameter β reflects that the efficiency of electron extraction from conduction band of the p-type ZnTe into the oxidizes (Scheme 1a) which is inversely associated with the diode ideality factor [57,58]. Thus, a value of 1 for the β corresponds to the ideal behavior. The obtained lower β value in this context implies serious recombination in both the ZnTe and ZTO-80 photocathodes via SS. Importantly, it is clear that for the ZTO-80 electrode a higher proportion of electrons enter the solution to participate in the reaction. As the voltage increases beyond − 1.7 V (vs. Fc^+/Fc), the electron Fermi energy level saturates near the conduction band position, leading to a gradual decrease in R_{ss} until it reaches stable values. Specifically, the values are 110 Ω for the ZTO-80 and 261 Ω for the ZnTe samples. At the same applied bias voltage, the R_{ss} shows a consistently lower value for the ZTO-80 compared to the ZnTe, indicating a reduction in the transfer resistance from the SS to the electrolyte.

The density of state (DOS) for the SS could be further derived from the $CPE_{ct,ss}$ based on the following relationship in Eq. (2).

$$C_\mu = q^2\frac{\partial n_{tot}}{\partial\mu_n} = q^2\frac{\partial(n_c + n_{ss})}{\partial\mu_n} \approx q^2\frac{\partial n_{ss}}{\partial E_F} \approx q^2N_{ss}(E) \tag{2}$$

where C_μ is the chemical capacitance per unit volume, $N_{ss}(E)$ is the DOS of SS as a function of potential [59,60]. Herein, the total electron density n_{tot} could be essentially simplified to the n_{ss} because the density of electrons n_{ss} released from the trapped state in the photocathode is much larger than that of free electrons n_c in the conduction band under the condition of $E_c - E_F \gg K_BT$. Thus, the chemical capacitance values (C_μ) derived from the impedance measurements correspond primarily to those charges correlated with the SS according to Eq. (2). As illustrated in Fig. 4c and S23, the energy distribution of DOS for the SS follows a Gaussian shape, being consistent with the Gaussian Disorder Model originally proposed by Bassler in Eq. 3.

$$N_{ss}(E) = \frac{N_t}{\sqrt{2\pi}\sigma}\exp\left[-\frac{(E_0 - E)^2}{2\sigma^2}\right] \tag{3}$$

where N_t is the total volume density of SS, E_0 is the center of the distribution and σ is the disorder parameter that gives the distribution

Table 1
The parameters obtained by fitting the curves of charge transfer resistance R_{ss} and chemical capacitance with Eqs. (1) and (3), which were obtained from impedance measurements on the ZTO-80 and the ZnTe photocathodes at different potentials.

	ZTO-80	ZnTe
β	0.17	0.07
N_t (cm^{-3})	1.82×10^{15}	2.18×10^{15}
E_0 (eV)	1.27	1.48
σ (eV)	0.24	0.55

width [61,62]. Table 1 lists the results (β, N_t, E_0, σ) by fitting R_{ss}, $N_{ss}(E)$ with Eqs. (2) and (3). As expected in materials affected by the structural or chemical defects, the intrinsic or extrinsic factors can introduce imperfections and distortions into the crystal structure, and the subsequent introduction of disorder into the crystal [63,64]. In the field of organic solar cells, this phenomenon significantly reduces the open circuit voltage and impacts the overall device performance [65,66]. The ZTO-80 based photocathode exhibited a significantly smaller disorder parameter σ value of 0.24 eV for the distribution width of DOS than that of the ZnTe-based photocathode (0.55 eV), which implies that the distribution of photogenerated carriers becomes more concentrated. Such a reduction in energy disorder in the ZTO-80 sample could be contributed to a reduction in non-radiative recombination losses as confirmed by PL measurements (Fig. S24) [67]. Reducing the energy disorder is beneficial for efficient electron extraction at the interface. Especially, the charge separation efficiency η_{se} is significantly increased from 25 % for the ZnTe to 61 % for the ZnTe-80 at -2.28 V (vs. Fc$^+$/Fc) in Fig. S25c. After the introduction of ZnO, the shift of E_0 implies a decrease in the required potential to fill the SS according to the Fermi-level pinning effect. Besides, we noted that there is insignificant order of magnitude change in N_t, indicating that introduction of ultrathin ZnO unchanged the number of carrier excitations in ZnTe. These improvements clearly verify that introduction of ZnO thin-layer results in efficient light-induced electron-hole separation and electrons transfer at the SEI.

This reduction in energy disorder (σ) leads to the narrowing of the localized state band tail (Scheme 1), a critical phenomenon that curtails the relaxation of non-equilibrium photo-generated carriers, especially at low-energy hopping sites [68,69]. This transition elevates the quasi-Fermi level of the electrons, boosting direct participation in reactions. By avoiding the loss of thermally trapped photoproduced carriers that are inefficient in participation, this mechanism ultimately enhances electron utilization [70]. This agrees well with the amplified charge separation efficiency and the heightened photo-generated current and overall FE in the ZTO-80 photocathode. In short, the ZnO effectively reduces the dangling bonds, retarding the recombination process and improving electron utilization.

Scanning electrochemical microscopy (SECM) is a highly valuable technique for studying the kinetics of heterogeneous charge transfer across various interfaces [71,72]. The apparent heterogeneous charge transfer rate constant κ and the effective heterogeneous charge transfer rate constant k_{eff} can be calculated by fitting the approach curves in Eqs. (4) and (5) (Fig. S26).

$$k_{eff} = \kappa \frac{D_{diffusion}}{r_T} \tag{4}$$

where $D_{diffusion}$ is the diffusion coefficient of the redox probe, r_T is the radius of Pt UME. The apparent standard electron transfer rate constant k_e^0 at the SEI can be further estimated by fitting the curves of $\ln(k_{eff})$ versus η according to Equation 6 (the Butler-Volmer model).

$$\ln(k_{eff}) = \ln k_e^0 - \alpha n f \eta \tag{5}$$

where α is the charge transfer coefficient in SECM, $f = nF/RT$, T is temperature, n is the number of electron transfer at the interface reaction, and η is the overpotential applied onto photocathode, respectively. Accordingly, the apparent standard electron transfer rate constant k_e^0 was estimated to be 10.48×10^{-2} cm s^{-1} for the ZTO-80 and 3.54×10^{-2} cm s^{-1} for the ZnTe by fitting the curves in Fig. 4d with a linear equation, respectively. The experimental data unequivocally demonstrate that the k_e^0 value for the ZTO-80 photocathode is almost three times higher than that of the ZnTe photocathode. Thus, owing to the presence of the ultra-thin ZnO layer in the ZTO-80 photocathode, the electrons originating from ZTO-80 exhibit superior kinetic properties in transferring to the acceptor at the SEI compared to those originating from pure ZnTe, which is consistent with the resistance slope

relationship (Fig. S27). The photoelectric injection efficiency (η_{inj}) of ZTO-80 is also improved to 81.28 % compared to its ZnTe counterpart 61.54 % at -2.28 V (vs. Fc$^+$/Fc) as delineated in Fig. S25d. Notably, the slow growth of η_{inj} with increasing potential on the ZnTe electrode may be due to the presence of deep energy level defects on the surface.

4. Conclusions

In this study, we reported a highly active ultrathin ZnO-modified ZnTe photocathode for PEC CO$_2$ reduction. The resulting photocathode exhibited an impressive photocurrent generation performance (-7.7 mA cm^{-2} at -2.58 V vs. Fc$^+$/Fc and -5.22 mA cm^{-2} at -2.28 V vs. Fc$^+$/Fc), high CO selectivity (93.88 %) and good stability (10 h) in CO$_2$-saturated acetonitrile with 0.1 M TBAPF$_6$ electrolyte. The ZnO-coated ZnTe surface improves the electron transfer coefficient (β) and increases the number of electrons involved in the reduction reaction, a process that is achieved mainly by reducing disorder (σ). This reduction in energy disorder leads to a narrowing of the localised state band tail, which reduces the loss of thermally trapped photo-generated carriers and improves electron utilization.

CRediT authorship contribution statement

Yan Wei: Writing – review & editing, Writing – original draft, Methodology, Investigation, Formal analysis, Data curation, Conceptualization. **Yanbin Zhu:** Investigation, Formal analysis. **Peize Li:** Data curation. **Xiaowu Gao:** Methodology, Investigation. **Zhaoshi Yu:** Methodology. **Shujie Liu:** Methodology. **Nan Li:** Data curation. **Yan Shen:** Writing – review & editing, Supervision, Project administration, Methodology, Formal analysis, Conceptualization. **Mingkui Wang:** Writing – review & editing, Methodology, Formal analysis, Data curation, Conceptualization.

Declaration of Competing Interest

The authors declare no competing financial interest.

Data availability

Data will be made available on request.

Acknowledgement

Appendix A. Supporting information

Supplementary data associated with this article can be found in the online version at doi:10.1016/j.apcatb.2024.123760.

References

[1] M. Grätzel, Photoelectrochemical cells, Nature 414 (2001) 338–344.
[2] J. Michl, Towards an artificial leaf? Nat. Chem. 3 (2011) 268–269.
[3] J. He, C. Janáky, Recent advances in solar-driven carbon dioxide conversion: expectations versus reality, ACS Energy Lett. 5 (2020) 1996–2014.
[4] V. Kumaravel, J. Bartlett, S. Pillai, Photoelectrochemical conversion of carbon dioxide (CO$_2$) into fuels and value-added products, ACS Energy Lett. 5 (2020) 486–519.

[5] P. Kempler, M. Richter, W. Cheng, B. Brunschwig, N. Lewis, Si microwire-array photocathodes decorated with Cu allow CO_2 reduction with minimal parasitic absorption of sunlight, ACS Energy Lett. 5 (2020) 2528–2534.

[6] J. Qiu, G. Zeng, M. Ha, M. Ge, Y. Lin, M. Hettick, B. Hou, A.N. Alexandrova, A. Javey, S.B. Cronin, Artificial photosynthesis on TiO_2-passivated InP nanopillars, Nano Lett. 15 (2015) 6177–6181.

[7] X. Deng, R. Li, S. Wu, L. Wang, J. Hu, J. Ma, W. Jiang, N. Zhang, X. Zheng, C. Gao, L. Wang, Q. Zhang, J. Zhu, Y. Xiong, Metal–organic framework coating enhances the performance of Cu_2O in photoelectrochemical CO_2 reduction, J. Am. Chem. Soc. 141 (2019) 10924–10929.

[8] U. Kang, S. Choi, D. Ham, S. Ji, W. Choi, D. Han, A. Abdel-Wahab, H. Park, Photosynthesis of formate from CO_2 and water at 1 % energy efficiency via copper iron oxide catalysis, Energy Environ. Sci. 8 (2015) 2638–2643.

[9] X. Chang, T. Wang, J. Gong, CO_2 photo-reduction: insights into CO_2 activation and reaction on surfaces of photocatalysts, Energy Environ. Sci. 9 (2016) 2177–2196.

[10] A. Pawar, C. Kim, M. Nguyen-Le, Y. Kang, General review on the components and parameters of photoelectrochemical system for CO_2 reduction with in situ analysis, ACS Sustain 7 (2019) 7431–7455.

[11] J. Jang, S. Cho, G. Magesh, Y. Jang, J. Kim, W. Kim, J. Seo, S. Kim, K. Lee, J. Lee, Aqueous-solution route to zinc telluride films for application to CO_2 reduction, Angew. Chem. Int. Ed. 53 (2014) 5852–5857.

[12] Y. Jang, M. Bhatt, J. Lee, S. Choi, B. Lee, J. Lee, Metal-free artificial photosynthesis of carbon monoxide using N-doped ZnTe nanorod photocathode decorated with N-doped carbon electrocatalyst layer, Adv. Energy Mater. 8 (2018) 1702636.

[13] Y. Jang, C. Lee, Y. Moon, S. Choe, Solar-driven syngas production using Al-doped ZnTe nanorod photocathodes, Materials 15 (2022) 3102.

[14] Y. Jang, J. Jang, J. Lee, J. Kim, H. Kumagai, J. Lee, T. Minegishi, J. Kubota, K. Domen, J. Lee, Selective CO production by Au coupled ZnTe/ZnO in the photoelectrochemical CO_2 reduction system, Energy Environ. Sci. 8 (2015) 3597–3604.

[15] Y. Jang, I. Jeong, J. Lee, J. Lee, M. Ko, J. Lee, Unbiased sunlight-driven artificial photosynthesis of carbon monoxide from CO_2 using a ZnTe-based photocathode and a perovskite solar cell in tandem, ACS Nano 10 (2016) 6980–6987.

[16] Q. Wang, X. Wang, Z. Yu, X. Jiang, J. Chen, L. Tao, M. Wang, Y. Shen, Artificial photosynthesis of ethanol using type-II g-C_3N_4/ZnTe heterojunction in photoelectrochemical CO_2 reduction system, Nano Energy 60 (2019) 827–835.

[17] L. Bertoluzzi, P. Lopez-Varo, J. Jiménez Tejada, J. Bisquert, Charge transfer processes at the semiconductor/electrolyte interface for solar fuel production: insight from impedance spectroscopy, J. Mater. Chem. A 4 (2016) 2873–2879.

[18] O. Zandi, T. Hamann, Enhanced water splitting efficiency through selective surface state removal, J. Phys. Chem. Lett. 5 (2014) 1522–1526.

[19] Y. Hu, Y. Pan, Z. Wang, T. Lin, Y. Gao, B. Luo, H. Hu, F. Fan, G. Liu, L. Wang, Lattice distortion induced internal electric field in TiO2 photoelectrode for efficient charge separation and transfer, Nat. Commun. 11 (2020) 2129.

[20] K. Kanazawa, S. Yoshida, H. Shigekawa, S. Kuroda, Dynamic probe of ZnTe (110) surface by scanning tunneling microscopy, Sci. Technol. Adv. Mater. 16 (2015) 015002.

[21] S. Tsukuda, M. Kita, T. Omata, $Zn(Te_{1-x}Se_x)$ quantum dots synthesized through a facile route and their band-edge and surface state driven visible-light emission, J. Lumin. 231 (2021) 117829.

[22] B. Klahr, S. Gimenez, F. Fabregat-Santiago, J. Bisquert, T.W. Hamann, Photoelectrochemical and impedance spectroscopic investigation of water oxidation with "Co–Pi"-coated hematite electrodes, J. Am. Chem. Soc. 134 (2012) 16693–16700.

[23] Z. Wang, F. Fan, S. Wang, C. Ding, Y. Zhao, C. Li, Bridging surface states and current–potential response over hematite-based photoelectrochemical water oxidation, RSC Adv. 6 (2016) 85582–85586.

[24] L. Bertoluzzi, L. Badia-Bou, F. Fabregat-Santiago, S. Gimenez, J. Bisquert, Interpretation of cyclic voltammetry measurements of thin semiconductor films for solar fuel applications, J. Phys. Chem. Lett. 4 (2013) 1334–1339.

[25] S. Giménez, J. Bisquert, In Photoelectrochemical Solar Fuel Production: From Basic Principles to Advanced Devices, Springer International Publishing, 2016.

[26] O. Zandi, T. Hamann, Determination of photoelectrochemical water oxidation intermediates on haematite electrode surfaces using operando infrared spectroscopy, Nat. Chem. 8 (2016) 778–783.

[27] J. Shi, X. Zhao, C. Li, Surface passivation engineering for photoelectrochemical water splitting, Catalysts 2 (2023) 271.

[28] H. Wang, Y. Xia, H. Li, X. Wang, Y. Yu, X. Jiao, D. Chen, Highly active deficient ternary sulfide photoanode for photoelectrochemical water splitting, Nat. Commun. 11 (2020) 3078.

[29] R. Liu, Z. Zheng, J. Spurgeon, X. Yang, Enhanced photoelectrochemical water-splitting performance of semiconductors by surface passivation layers, Energy Environ. Sci. 7 (2014) 2504–2517.

[30] G. Liu, J. Eichhorn, C. Jiang, M. Scott, L. Hess, J. Gregoire, J. Haber, I. Sharp, F. Toma, Interface engineering for light-driven water oxidation: unravelling the passivating and catalytic mechanism in BiVO4 overlayers, Sustain. Energy Fuels 3 (2019) 127–135.

[31] Z. Yu, L. Chen, L. Luo, R. Huang, Z. Tang, P. Xiao, Y. Zhang, Combining bulk charge transport and surface charge transfer to design titanium-doped hematite homojunction photoanodes, J. Phys. Chem. C 126 (2022) 4296–4305.

[32] Q. Shi, S. Murcia-López, P. Tang, C. Flox, J.R. Morante, Z. Bian, H. Wang, T. Andreu, Role of tungsten doping on the surface states in BiVO4 photoanodes for water oxidation: tuning the electron trapping process, ACS Catal. 8 (2018) 3331–3342.

[33] Y. Gao, T. Hamann, Elucidation of CuWO4 surface states during photoelectrochemical water oxidation, J. Phys. Chem. Lett. 8 (2017) 2700–2704.

[34] P. Varadhan, H. Fu, D. Priante, J.R.D. Retamal, C. Zhao, M. Ebaid, T.K. Ng, I. Ajia, S. Mitra, I.S. Roqan, B.S. Ooi, J.-H. He, Surface passivation of GaN nanowires for enhanced photoelectrochemical water-splitting, Nano Lett. 17 (2017) 1520–1528.

[35] Y. Liu, M. Xia, D. Ren, S. Nussbaum, J. Yum, M. Grätzel, K. Guijarro, K. Sivula, Photoelectrochemical CO_2 reduction at a direct CuInGaS2/electrolyte junction, ACS Energy Lett. 8 (2023) 1645–1651.

[36] X. Teng, J. Lu, Y. Niu, S. Gong, M. Xu, T.J. Meyer, Z. Chen, Selective CO_2 reduction to formate on a Zn-based electrocatalyst promoted by tellurium, Chem. Mater. 34 (2022) 6036–6047.

[37] Y. Zhou, L. Xu, J. Wu, W. Zhu, T. He, H. Yang, H. Huang, T. Cheng, Y. Liu, Z. Kang, The operation active sites of O_2 reduction to H_2O_2 over ZnO, Energy Environ. Sci. 16 (2023) 3526–3533.

[38] J. Guerrero, E. Bajard, N. Schneider, F. Dumoulin, D. Lincot, U. Isci, M. Robert, N. Naghavi, Multifunctional photovoltaic window layers for solar-driven catalytic conversion of CO_2: the case of CIGS solar cells, ACS Energy Lett. 8 (2023) 3488–3493.

[39] M. Wang, A. Kafizas, S. Sathasivam, M. Blunt, B. Moss, S. Gonzalez-Carrero, C. Carmalt, ZnO/BiOI heterojunction photoanodes with enhanced photoelectrochemical water oxidation activity, Appl. Catal. B 331 (2023) 122657.

[40] Y. Liu, M. Bouri, L. Yao, M. Xia, M. Mensi, M. Grätzel, K. Sivula, U. Aschauer, N. Guijarro, Identifying reactive sites and surface traps in chalcopyrite photocathodes, Angew. Chem. Int. Ed. 2021 (60) (2021) 23651–23655.

[41] Y. Liu, G. Xong, W. Chen, H. Su, Y. Liu, F. Cai, G. Wang, J. Zeng, Oxygen vacancies in ZnO nanosheets enhance CO_2 electrochemical reduction to CO, Angew. Chem. Int. Ed. 57 (2018) 6054–6059.

[42] D. Ren, J. Gao, L. Pan, Z. Wang, J. Luo, S.M. Zakeeruddin, A. Hagfeldt, M. Grätzel, Atomic layer deposition of ZnO on CuO enables selective and efficient electroreduction of carbon dioxide to liquid fuels, Angew. Chem. Int. Ed. 58 (2019) 15036–15040.

[43] S. Zhang, L. Qiu, Y. Zheng, Q. Shi, T. Zhou, V. Sencadas, Y. Xu, S. Zhang, L. Zhang, C. Zhang, C. Zhang, S. Yu, Z. Guo, Rational design of core-shell ZnTe@N-doped carbon nanowires for high gravimetric and volumetric alkali metal ion storage, Adv. Funct. Mater. 31 (2021) 2006425.

[44] M.F. Ehsan, T. He, In situ synthesis of ZnO/ZnTe common cation heterostructure and its visible-light photocatalytic reduction of CO_2 into CH_4, Appl. Catal. B 166–167 (2015) 345–352.

[45] Y. Liu, Z. Kang, Z. Chen, I. Shafiq, J. Zapien, I. Bello, W. Zhang, S. Lee, Synthesis, characterization, and photocatalytic application of different ZnO nanostructures in array configurations, Cryst. Growth Des. 9 (2009) 3222–3227.

[46] H. Qian, H. Tong, L. Zhou, B. Yan, H. Ji, K. Xue, X. Cheng, X. Miao, Low work function of crystalline GeTe/Sb2Te3 superlattice-like films induced by Te dangling bonds, J. Phys. D 49 (2016) 495302.

[47] F. Xu, K. Meng, B. Cheng, S. Wang, J. Xu, J. Yu, Unique S-scheme heterojunctions in self-assembled TiO2/CsPbBr3 hybrids for CO_2 photoreduction, Nat. Commun. 11 (2020) 4613.

[48] T. Li, T. Kasahara, J. He, K.E. Dettelbach, G. Sammis, C. Berlinguette, Photoelectrochemical oxidation of organic substrates in organic media, Nat. Commun. 8 (2017) 390.

[49] M. Kang, C. Kim, A. Pawar, H. Cha, S. Ji, W. Cai, Y.S. Kang, Selective alcohol on dark cathodes by photoelectrochemical CO_2 valorization and their in situ characterization, ACS Energy Lett. 4 (2019) 1549–1555.

[50] I. Taniguchi, B. Aurian-Blajeni, J. Bockris, The reduction of carbon dioxide at illuminated p-type semiconductor electrodes in nonaqueous media, Electrochim. Acta 29 (1984) 923–932.

[51] D. Monllor-Satoca, M. Bärtsch, C. Fàbrega, A. Genç, S. Reinhard, T. Andreu, J. Arbiol, M. Niederberger, J. Morante, What do you do, titanium? Insight into the role of titanium oxide as a water oxidation promoter in hematite-based photoanodes, Energy Environ. Sci. 8 (2015) 3242–3254.

[52] J. Krýsa, T. Imrich, Š. Paušová, H. Krýsová, M. Neumann-Spallart, Hematite films by aerosol pyrolysis: Influence of substrate and photocorrosion suppression by TiO2 capping, Catal. Today 335 (2019) 418–422.

[53] Y. Jang, M. Bhatt, J. Lee, S. Choi, B. Lee, J. Lee, Metal-free artificial photosynthesis of carbon monoxide using N-doped ZnTe nanorod photocathode decorated with N-doped carbon electrocatalyst layer, Adv. Energy Mater. 8 (2018) 1702636.

[54] P. Wen, H. Li, X. Ma, R. Lei, X. Wang, S.M. Geyer, Y. Qiu, A colloidal ZnTe quantum dot-based photocathode with a metal–insulator–semiconductor structure towards solar-driven CO_2 reduction to tunable syngas, J. Mater. 9 (2021) 3589–3596.

[55] B. Klahr, S. Gimenez, F. Fabregat-Santiago, T. Hamann, J. Bisquert, Photoelectrochemical and impedance spectroscopic investigation of water oxidation with "Co–Pi"-coated hematite electrodes, J. Am. Chem. Soc. 134 (9) (2012) 4294–4302.

[56] J. Bisquert, Theory of the impedance of electron diffusion and recombination in a thin layer, J. Phys. Chem. B 106 (2002) 325–333.

[57] J. Bisquert, I. Mora-Seró, Simulation of steady-state characteristics of dye-sensitized solar cells and the interpretation of the diffusion length, J. Phys. Chem. Lett. 1 (2009) 450–456.

[58] F. Fabregat-Santiago, G. Garcia-Belmonte, I. Mora-Sero, J. Bisquert, Characterization of nanostructured hybrid and organic solar cells by impedance spectroscopy, Phys. Chem. Chem. Phys. 13 (2011) 9083–9118.

[59] J. Bisquert, Chemical capacitance of nanostructured semiconductors: its origin and significance for nanocomposite solar cells, Phys. Chem. Chem. Phys. 5 (2003) 5360–5364.

[60] J. Bisquert, A. Zaban, M. Greenshtein, I. Mora-Seró, Determination of rate constants for charge transfer and the distribution of semiconductor and electrolyte electronic energy levels in dye-sensitized solar cells by open-circuit photovoltage decay method, J. Am. Chem. Soc. 126 (2004) 13550–13559.

[61] J. Bisquert, F. Fabregat-Santiago, I. Mora-Seró, G. Garcia-Belmonte, E. Barea, E. Palomares, A review of recent results on electrochemical determination of the density of electronic states of nanostructured metal-oxide semiconductors and organic hole conductors, Inorg. Chim. Acta 361 (2008) 684–698.

[62] H. Bässler, Charge transport in disordered organic photoconductors a Monte Carlo simulation study, Phys. Status Solidi B Basic. Res. 175 (1993) 15–56.

[63] Y. Jiang, J. Wang, H. Zai, D. Ni, J. Wang, P. Xue, N. Li, B. Jia, H. Lu, Y. Zhang, F. Wang, Z. Guo, Z. Bi, H. Xie, Q. Wang, W. Ma, Y. Tu, H. Zhou, X. Zhan, Reducing energy disorder in perovskite solar cells by chelation, J. Am. Chem. Soc. 15 (7) (2022) 2806–2818.

[64] J. Yuan, C. Zhang, B. Qiu, W. Liu, S.K. So, M. Mainville, M. Leclerc, S. Shoaee, D. Neher, Y. Zou, Effects of energetic disorder in bulk heterojunction organic solar cells, Energy Environ. Sci. 15 (2022) 2806–2818.

[65] G. Xu, R. Xue, S. Stuard, H. Ade, C. Zhang, J. Yao, Y. Li, Y. Li, Reducing energy disorder of hole transport layer by charge transfer complex for high performance p–i–n perovskite solar cells, Adv. Mater. 33 (2021) e2006753.

[66] N.K. Elumalai, A. Uddin, Open circuit voltage of organic solar cells: an in-depth review, Energy Environ. Sci. 9 (2016) 391–410.

[67] Y. Jiang, J. Wang, H. Zai, D. Ni, J. Wang, P. Xue, N. Li, B. Jia, H. Lu, Y. Zhang, F. Wang, Z. Guo, Z. Bi, H. Xie, Q. Wang, W. Ma, Y. Tu, H. Zhou, X. Zhan, Reducing energy disorder in perovskite solar cells by chelation, J. Am. Chem. Soc. 144 (2022) 5400–5410.

[68] Y. Shao, Y. Yuan, J. Huang, Correlation of energy disorder and open-circuit voltage in hybrid perovskite solar cells, Nat. Energy 1 (2016) 15001.

[69] R. Coehoorn, W.F. Pasveer, P.A. Bobbert, M.A.J. Michels, Charge-carrier concentration dependence of the hopping mobility in organic materials with Gaussian disorder, Phys. Rev. B 72 (2005) 155206.

[70] Y. Deng, F. Peng, Y. Lu, X. Zhu, W. Jin, J. Qiu, J. Dong, Y. Hao, D. Di, Y. Gao, T. Sun, M. Zhang, F. Liu, L. Wang, L. Ying, F. Huang, Y. Jin, Solution-processed green and blue quantum-dot light-emitting diodes with eliminated charge leakage, Nat. Photonics 16 (2022) 505–511.

[71] B. Zhang, H. Yuan, X. Zhang, D. Huang, S. Li, M. Wang, Y. Shen, Investigation of regeneration kinetics in quantum-dots-sensitized solar cells with scanning electrochemical microscopy, ACS Appl. Mater. Interfaces 6 (2014) 20913–20918.

[72] B. Zhang, X. Zhang, X. Xiao, Y. Shen, Photoelectrochemical water splitting system—a study of interfacial charge transfer with scanning electrochemical microscopy, ACS Appl. Mater. Interface 8 (2016) 1606–1614.